ACSNANO

www.acsnano.org

ARTICLE

Robust Multicolor Single Photon Emission from Point Defects in Hexagonal Boron Nitride

Toan Trong Tran,[†] Christopher Elbadawi,[†] Daniel Totonjian,[†] Charlene J. Lobo,[†] Gabriele Grosso,[‡] Hyowon Moon,[‡] Dirk R. Englund,[‡] Michael J. Ford,[†] Igor Aharonovich,[*,†] and Milos Toth[*,†]

[†]School of Mathematical and Physical Sciences, University of Technology Sydney, Ultimo, New South Wales 2007, Australia

[‡]Department of Electrical Engineering and Computer Science, Massachusetts Institute of Technology, Cambridge, Massachusetts 02139, United States

Supporting Information

ABSTRACT: **Hexagonal boron nitride (hBN) is an emerging two-dimensional material for quantum photonics owing to its large bandgap and hyperbolic properties. Here we report two approaches for engineering quantum emitters in hBN multilayers using either electron beam irradiation or annealing and characterize their photophysical properties. The defects exhibit a broad range of multicolor room-temperature single photon emissions across the visible and the near-infrared spectral ranges, narrow line widths of sub-10 nm at room temperature, and a short excited-state lifetime, and high brightness. We show that the emitters can be categorized into two general groups, but most likely possess similar crystallographic structure. Remarkably, the emitters are extremely robust and withstand aggressive annealing treatments in oxidizing and reducing environments. Our results constitute a step toward deterministic engineering of single emitters in 2D materials and hold great promise for the use of defects in boron nitride as sources for quantum information processing and nanophotonics.**

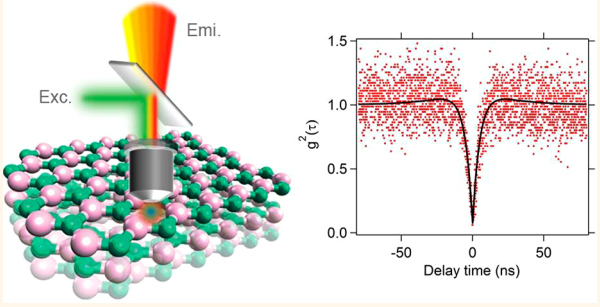

KEYWORDS: *single photon source, hexagonal boron nitride, point defects, robust, electron beam irradiation, density functional theory*

Hexagonal boron nitride (hBN) is a van der Waals material that has recently emerged as a fascinating platform for room-temperature quantum photonics due to the discovery of room-temperature quantum emitters,[1] realization of subdiffraction focusing and guiding,[2,3] super-resolution imaging,[4] and tunable phonon polariton propagation.[5,6] While the optical properties of bulk hBN have been studied thoroughly,[7−9] detailed photophysical properties of its two-dimensional (2D) counterpart are scarce. In particular, the luminescent properties of hBN under sub-band gap excitation remain largely unexplored.

In traditional 3D semiconductors, including diamond and silicon carbide, color centers have similar spectral properties in both bulk and nanostructured forms. This may be advantageous when controlled engineering of defects is required. Both materials can be doped during growth, resulting in deterministic formation of luminescent centers. However, in van der Waals crystals, the electronic and optical properties of 2D (single or few monolayer) flakes are significantly different from their bulk counterparts.[10] This often results in fascinating phenomena such as spin valley splitting[11] or strong exciton−phonon interactions that can be observed at room temperature,[12] but poses major challenges for engineering and control of single color centers.

In this work, we show that single emitters in hBN can be engineered using electron irradiation and withstand various aggressive annealing treatments in reactive gaseous environments, which do not change their spectral properties. We characterize the emitters and report an interesting phenomenon, namely, narrowband multicolor single photon emission from a 2D material. While known color centers and standard quantum dots (of a given, fixed chemical composition) luminess at a particular wavelength or over a narrow spectral range, we show that defects in hBN multilayers can emit over a broad range spanning over 200 nm. We also show that the emitters withstand various aggressive annealing treatments in reactive gaseous environments, which do not change their spectral properties. Our results pave the way to robust, room-temperature quantum photonic devices that employ color centers in hBN as key building blocks.

RESULTS AND DISCUSSION

We developed two different processes for engineering of the emitters, based on annealing and electron beam irradiation,

Received: June 1, 2016
Accepted: July 11, 2016
Published: July 11, 2016

DOI: 10.1021/acsnano.6b03602
ACS Nano 2016, 10, 7331−7338

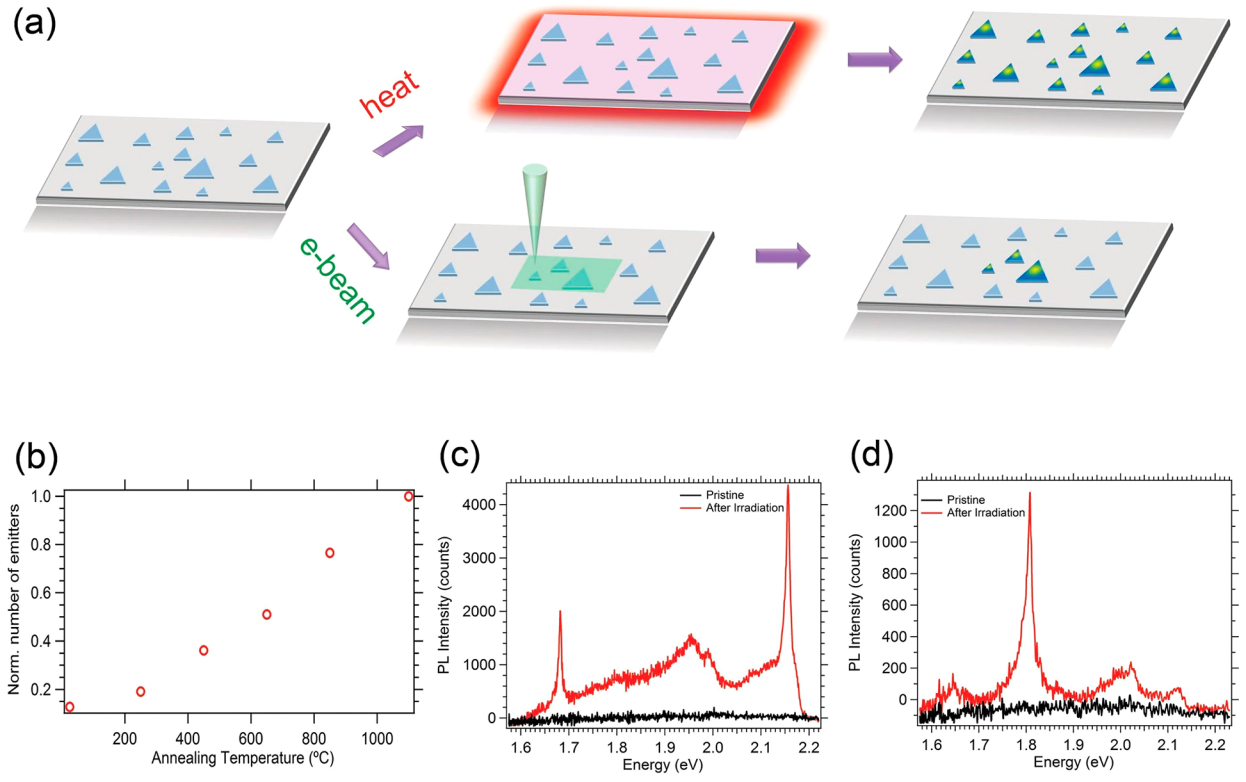

Figure 1. Generation of emitters in hBN. (a) Schematic illustration of two independent processes that yield emitters: annealing and electron beam irradiation. As-grown, dropcast hBN flakes are either annealed in an argon environment or irradiated by an electron beam in a low vacuum H_2O environment. (b) Normalized number of stable, bright single emitters as a function of annealing temperature found in hBN multilayers. Each data point was taken from a unique sample that was annealed at a single temperature. (c,d) Examples of PL spectra from emitters fabricated by an electron beam. Each pair shows data recorded from a fixed sample region before (black curve) and after (red curve) electron irradiation.

illustrated schematically in Figure 1a. Either method can be used to create the studied defects in hBN. The annealing method was optimized by varying the annealing temperature of as-grown flakes in an inert environment. Each annealing treatment was performed for 30 min under 1 Torr of argon. Figure 1b shows that the number of stable color centers found by confocal PL increases with annealing temperature, indicating that defect diffusion and lattice relaxation occur in the flakes. This behavior is similar to the well-studied nitrogen vacancy center in diamond.[13,14]

The second process involves electron beam irradiation performed using a scanning electron microscope. The as-grown flakes were first deposited on a silicon substrate and precharacterized by confocal PL mapping (see Figure S1) and spectroscopy. Then, particular sample regions were irradiated by a 15 keV, 1.4 nA electron beam for 1 h in a low vacuum, H_2O vapor environment[15] (the H_2O prevents electron beam deposition of carbon[16] that is luminescent and modifies PL spectra). A detailed description of the irradiation experiments is provided in the Methods section. There were no changes in Raman spectra of the flakes after these treatments. This observation is not unexpected considering the high stability of hBN flakes.[17] The precharacterized sample regions were then remeasured using the confocal PL microscope. Figure 1c,d shows photoluminescence (PL) spectra recorded before (black curve) and after electron irradiation (red curve) from two sample regions. Luminescent defects were created by the electron beam in each case. Importantly, no annealing was performed before or after the electron beam irradiation treatments. Our results therefore demonstrate two distinct robust methodologies for engineering of the emitters in hBN.

Next, we proceeded to study the stability of the emitters in various gaseous environments. These properties are important both from a technological point of view, since the emitters can potentially be used as sensors or quantum light sources in harsh chemical environments, and for understanding their chemical origin, as annealing in different gases can modify defect emission properties.[18,19] First, we leveraged the defect fabrication study (Figure 1b) to create emitters by annealing a sample for 30 min in Ar at 850 °C. The sample was then characterized by confocal PL, annealed sequentially at 500 °C for 1 h each in hydrogen, oxygen, and ammonia environments, and recharacterized by PL after each annealing step. To provide a direct comparison, we selected two specific defects (located using a grid) with different photon energies and compared their spectra and second-order autocorrelation functions before and after annealing in different environments. Spectra from two stable emitters are shown in Figure 2a,c, respectively (the emitters belong to two groups defined below and in Figure S2). The fluorescence from the emitters remains unmodified even after annealing in both oxidizing and reducing environments. Figure 2b,d shows corresponding autocorrelation $g^2(\tau)$ curves for the two emitters (see Figure 3 and the Supporting Information for experimental details) recorded for each emitter after the initial argon annealing treatment (black curve) and after the final annealing step performed in an ammonia environment (red curve). All autocorrelation curves show that $g^2(0) < 0.5$, proving unambiguously that the emitters are point

DOI: 10.1021/acsnano.6b03602
ACS Nano 2016, 10, 7331−7338

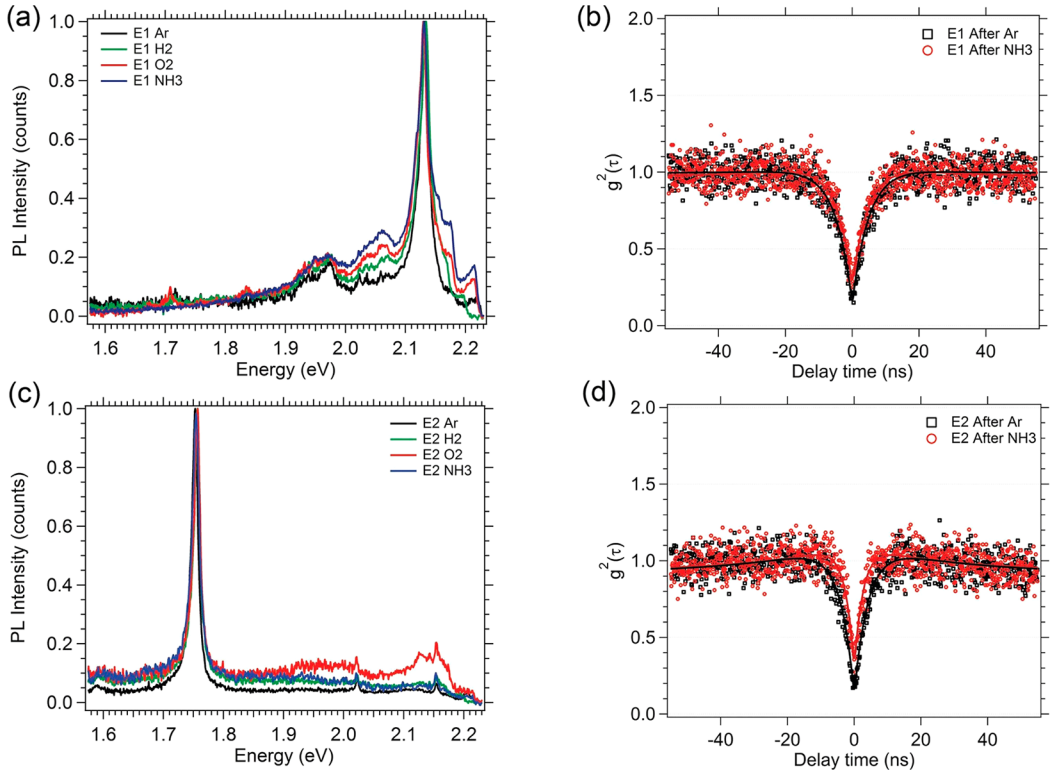

Figure 2. Stability of the emitters. (a,c) Normalized luminescence recorded at room temperature from two emitters (E1 and E2) after sequential annealing in argon, hydrogen, oxygen, and ammonia. (b,d) Corresponding antibunching measurements proving that the quantum nature of the defects persists after the sequential set of 30 min anneals performed in H_2, O_2, and NH_3 environments. Emitters E1 and E2 belong to Groups 1 and 2, respectively. The groups are defined in Figure 3.

defects that act as single photon sources. The data convincingly prove the robustness of the emitters and the persistence of their quantum nature.

The annealing results provide important insights into the nature of the emitters. First, the luminescent defect is likely to have a vacancy in its crystallographic structure. This is because of the clear increase in formation probability with annealing temperature, a behavior that is very typical of vacancy-related complexes in solids.[14,20] Second, it is likely that the emitters are charge neutral. If the emitters were negatively charged, annealing in a hydrogen environment would have been expected to modify the charge state and modify or eliminate the emission. This behavior is exemplified by the NV center in diamond which switches from the negative to the neutral charge state upon annealing in hydrogen (and *vice versa* upon annealing in oxygen).[14,20] Similarly, many negatively charged emitters in GaN are switched off upon annealing in hydrogen.[21] Positively charged defects are not considered, as to the best of our knowledge, positively charged single photon emitters in solids have not been observed. Finally, we believe that the emitters that are stable upon annealing cannot be surface states, as has been observed for some TMDs.[22] This is because surface states are often unstable and are expected to be modified upon annealing in different reactive environments. We note, however, that while many of the emitters were absolutely stable and resisted all the annealing treatments, each annealing step did create some new emitters and quench some emitters. Both of these effects are demonstrated in Figure S3 and are not surprising, as is discussed in the Supporting Information.

Figure 3a shows a simplified schematic of the confocal PL setup used to characterize hBN. A detailed schematic and a typical confocal map featuring a number of single photon emitters are shown in Figure S1. Unless noted otherwise, the measurements were performed at room temperature using either a 532 nm continuous-wave (CW) laser or a 510 nm pulsed laser as an excitation source for lifetime measurements. We performed a PL survey and collected spectra of various single defect centers in hBN (which was annealed previously in argon at 850 °C, as is discussed below). A representative range of room-temperature PL spectra is shown in Figure 3b, c. The emitters have narrow zero phonon lines (ZPLs) at energies in the range of ~1.6−2.2 eV (~565−775 nm).

The emitters can be classified into two general groups based on their ZPL energy and phonon sideband (PSB) spectral shapes. Group 1 (Figure 3b) consists of emitters with ZPL energies of 576 nm (2.15 eV), 583 nm (2.13 eV), 602 nm (2.06 eV), 633 nm (1.96 eV), and 652 nm (1.90 eV). Emitters in this group exhibit relatively broad and asymmetric ZPL line shapes with pronounced low-energy tails. The spectra also contain pronounced doublet PSBs. Group 2 (Figure 3c) is comprised of emitters at lower energies, with ZPLs centered on 681 nm (1.82 eV), 696 nm (1.78 eV), 714 nm (1.74 eV), and 762 nm (1.63 eV). Notably, these emitters have narrower, more symmetric ZPLs, with phonon sidebands that are weak compared to Group 1. A survey of ~40 emitters (Figure S2a−e) in the sample annealed at 850 °C revealed a relative abundance of ~70% and 30% of emitters in Groups 1 and 2, respectively. Figure 3d is a histogram showing the ZPL energies of emitters classified into the two groups.

A Hanbury, Brown, and Twiss (HBT) setup was used to verify single photon emission from these defects. Figure 3e shows second-order autocorrelation functions ($g^2(\tau)$) recorded

DOI: 10.1021/acsnano.6b03602
ACS Nano 2016, 10, 7331−7338

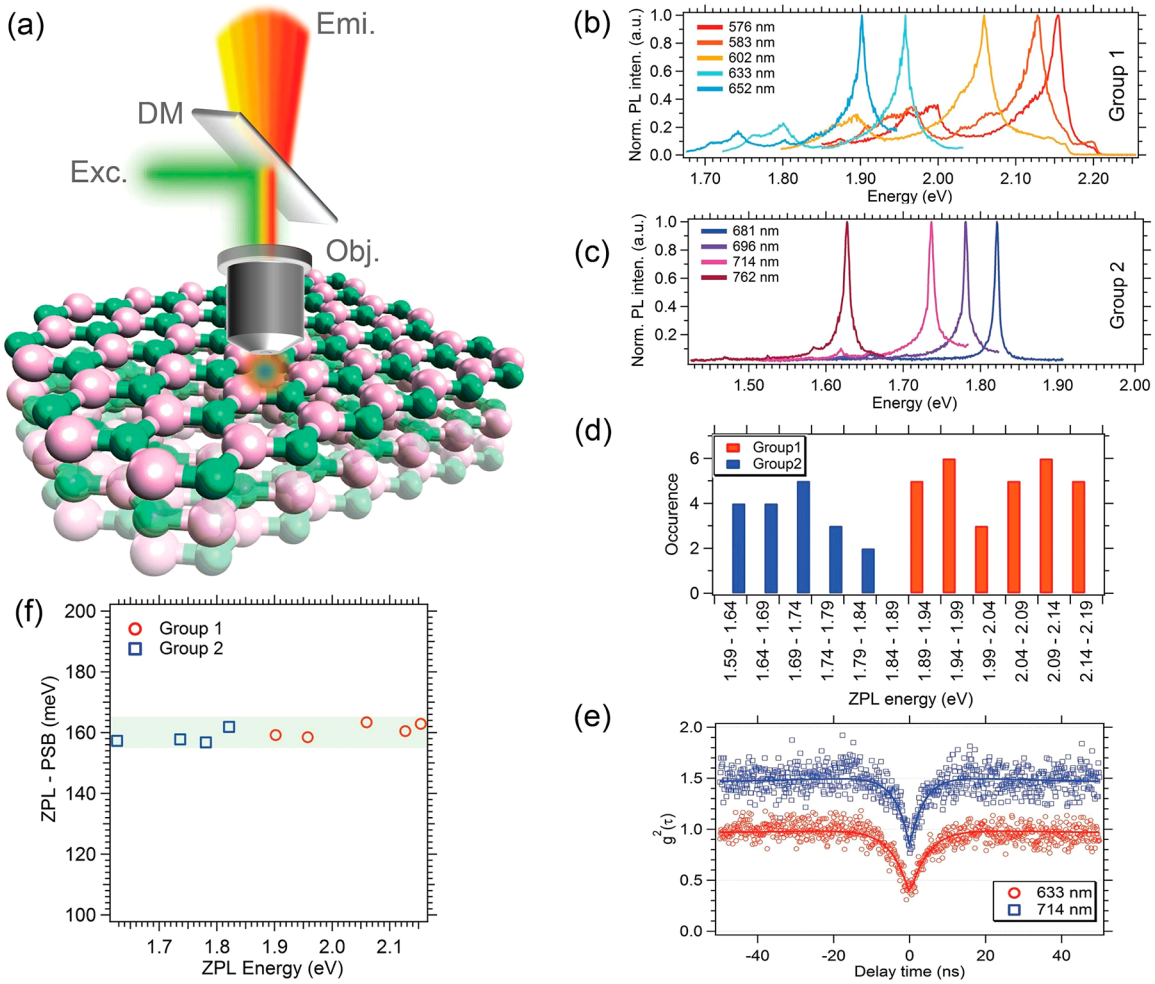

Figure 3. Multicolor PL from point defects in hBN. (a) Simplified schematic of the PL setup showing the excitation and emission of a defect center in a hBN lattice. The objective lens, dichroic mirror, excitation source, and emission are denoted by Obj., DM, Exc., and Emi., respectively. (b) Five examples of emitters in Group 1 with ZPLs at 576 nm (2.15 eV), 583 nm (2.13 eV), 602 nm (2.06 eV), 633 nm (1.96 eV), and 652 nm (1.90 eV). (c) Four examples of emitters in Group 2 with ZPLs at 681 nm (1.82 eV), 696 nm (1.78 eV), 714 nm (1.74 eV), and 762 nm (1.63 eV). (d) Histogram of ZPL energy for numerous emitters in Groups 1 (red) and 2 (blue). Each spectrum was acquired from a separate sample region at room temperature using a 300 μW CW 532 nm laser. (e) Second-order autocorrelation functions showing that $g^2(0)$ = 0.39 and 0.34, respectively. The $g^2(\tau)$ functions were acquired using an excitation power of 300 μW and an acquisition time of 20 s and were normalized (without background correction) and offset vertically for clarity. A neutral density filter was used to attenuate the signal generated by the 633 nm emitter. (f) Difference in the energy of the ZPL and PSB *versus* ZPL energy. The shaded band in (f) is a guide to the eye. In (b) and (c), high-energy portions of some spectra were cut from the graph for clarity, to avoid overlaps between the spectra.

from representative emitters selected from each group, with ZPLs centered on 633 nm (Group 1 emitter) and 714 nm (Group 2 emitter). Both curves show that $g^2(0) < 0.5$, proving unambiguously that the defects are point defects that act as single photon emitters (an additional $g^2(\tau)$ from each group is shown in Figure S2f,g). The data were not background-corrected,[23] fit using a three level model, and offset vertically for clarity.

To calculate phonon mode energies coupled to the emission channel, we record the difference in energy between the ZPL maximum and the highest intensity measured in the PSB of each emitter. It is important to note that emitters in both groups exhibit a similar energy gap difference of 160 ± 5 meV between the ZPL and the PSB (Figure 3f). These values indicate that the associated coupled localized vibrations (phonon modes) are very similar, and the defects responsible for all spectra have similar crystallographic structure.[24,25] Hence, the two groups likely correspond to two similar defects that reside in different local dielectric environments. The variation in ZPL position within each group may be contributed to variations in local strain and dielectric environment, as is discussed below. We note that the spectra of emitters in Group 1 are very similar to those of a color center that was previously ascribed to the NBVN defect in hBN.[1]

Next, we present a detailed analysis of the photophysical properties of the two emitters whose $g^2(\tau)$ curves are shown in Figure 3e, which are representative of emitters in each of the two groups shown in Figure 3b,c. To obtain the optical transition lifetimes of these emitters, we performed a time-resolved fluorescence measurement using a 510 nm pulsed laser with a 20 MHz repetition rate and 100 ps pulse width. As is seen in Figure 4a, the lifetimes of the two emitters were extracted using single exponential fits, yielding values of 2.9 and 6.7 ns for the centers with ZPLs at 633 and 714 nm, respectively (the onsets of the decay curves should be ignored

DOI: 10.1021/acsnano.6b03602
ACS Nano 2016, 10, 7331−7338

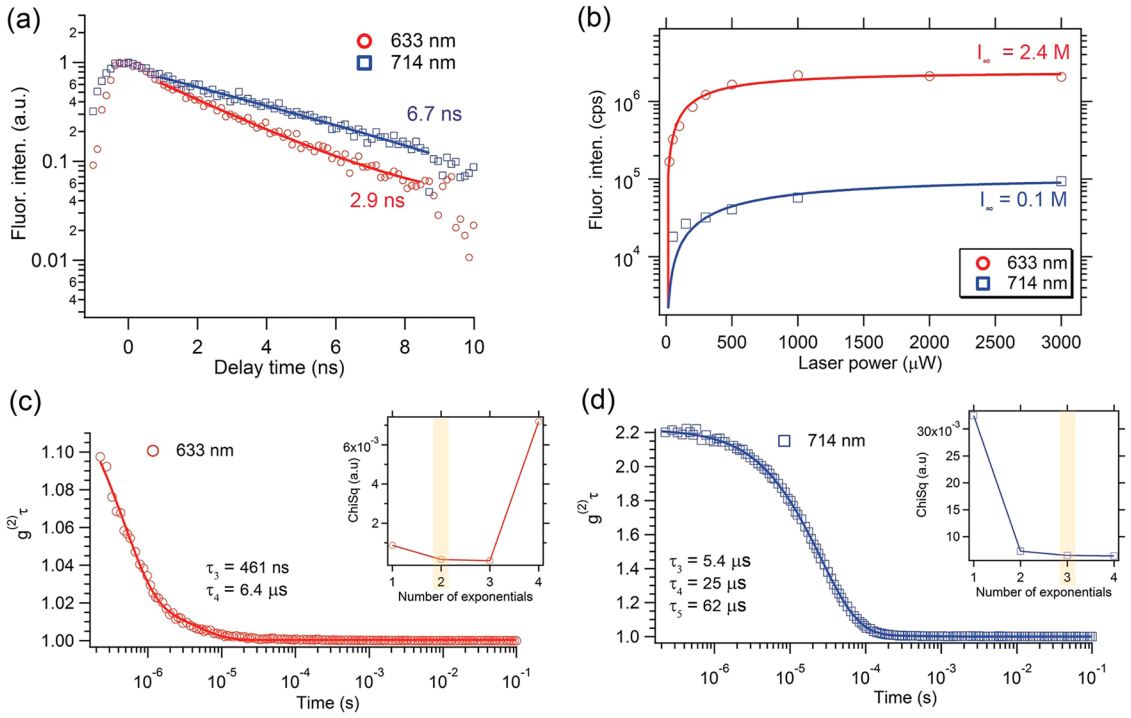

Figure 4. Photophysical properties of the defects. (a) Time-resolved fluorescence measurements showing radiative transition lifetimes of the emitters. A 80 μW, 510 nm pulsed laser with a repetition rate of 20 MHz and a pulse width of 100 ps was used as the excitation source. The solid lines are fits obtained using single exponential decay functions. (b) Fluorescence saturation curves and corresponding theoretical fits calculated using a three level model. (c,d) Second-order autocorrelation function, $g^2(\tau)$, recorded over a longer time scale from the two color centers presented in Figure 1 with ZPLs at (c) 633 and (d) 714 nm. The corresponding solid traces are theoretical fits to the experimental data. Insets show the fitting residue χ^2 *versus* the number of exponentials used in the fitting functions. The yellow bands indicate optimal fits realized when the number of exponentials and the residues are simultaneously minimized.

since they correspond to the response of our experimental setup).

Fluorescence saturation behavior was characterized by measuring PL intensity as a function of excitation power. The results are shown in Figure 4b, and the data were fit using the expression: $I = I_\infty P/(P + P_0)$, where I_∞ and P_{sat} are the emission rate and excitation power at saturation,[26] respectively. The resulting emission rates at saturation for the 633 and 714 nm emitters are 2.4×10^6 and 0.1×10^6 counts/s, at P_{sat} = 310 μW and 770 μW, respectively.

To gain further insights into the observed variation in emitter brightness, we measured the autocorrelation functions over longer time scales up to 0.1 s. These measurements provide information about the presence of other metastable states with longer decay times.[27−29] Figure 4c,d shows long time scale photon antibunching curves for the two color centers. By applying an increasing number of components in the multiexponential fitting function, we obtained a fitting function with a least number of exponentials and lowest fitting residue χ^2 for each center. Table 1 summarizes the additional decay lifetimes obtained from the fits.

Table 1. Additional Metastable States Associated with the Investigated Emitters

	ZPL = 633 nm	ZPL = 714 nm
τ_3 [μs]	0.46	5.4
τ_4 [μs]	6.4	25
τ_5 [μs]	–	62

These measurements account for the difference in the overall brightness of the two emitters. The brighter 633 nm defect has fewer metastable states with shorter lifetimes, while the 714 nm defect exhibits multiple additional metastable states with relatively long lifetimes. The differences in lifetimes of both radiative and nonradiative transitions between the two emitters are indicative of local environmental effects such as the presence of neighboring impurities or the proximity of a center to the surface or the edge of a multilayer hBN flake.

To further characterize the photodynamics of these emitters, we obtained photon antibunching curves *versus* excitation power (Figure S4). By fitting the data using the three-level model[30] $g^{(2)}(\tau) = c - ae^{-\tau/\tau 1} + be^{-\tau/\tau 2}$, we obtained the power-dependent emission lifetimes, τ_1, and mestastable state lifetimes, τ_2, as a function of excitation power.[31−33] The corresponding lifetimes $\tau^0{}_1$ and $\tau^0{}_2$ were then obtained by extrapolating the data to zero excitation power,[31−33] (Figure S5) yielding the values $\tau^0{}_1$ = 3.3 and 8.1 ns and $\tau^0{}_2$ = 88.6 and 1.2 ns for the 633 and 714 nm emitters, respectively. The $\tau^0{}_1$ values are in good agreement with those obtained by the direct time-resolved fluorescence lifetime measurements discussed earlier.

Finally, we obtained spectra of emitters from each group at cryogenic temperatures. Figure 5a,b shows room-temperature and low-temperature (14 K) spectra from emitters in Groups 1 and 2, respectively. As expected, the line width is dramatically reduced and approaching 3.87 and 1.17 meV for emitters in Groups 1 and 2, respectively. The spectra at low temperature confirm the difference in the ZPL shape for the two groups. In particular, the asymmetry of the ZPL in group 1 is maintained

DOI: 10.1021/acsnano.6b03602
ACS Nano 2016, 10, 7331−7338

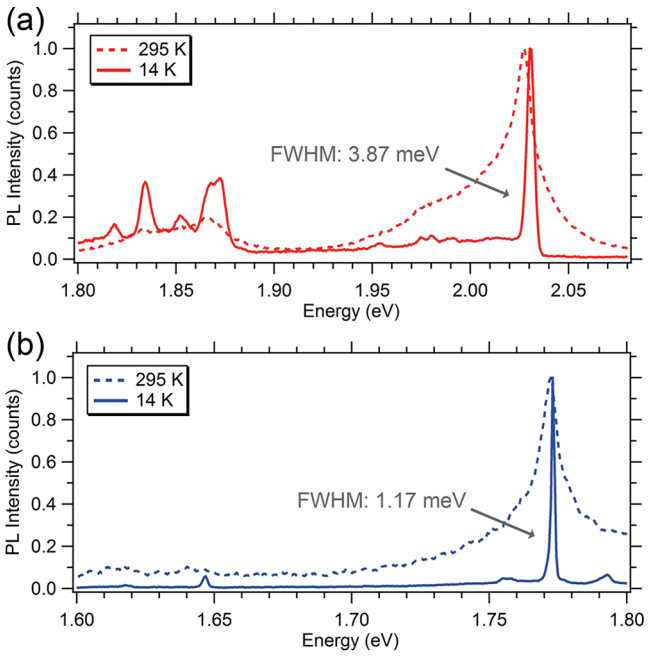

Figure 5. Room- and low-temperature (295 and 14 K, respectively) spectra of representative emitters from Groups (a) 1 (dashed and solid red traces) and (b) 2 (dashed and solid blue traces), respectively. At 14 K the line widths approach 3.87 and 1.17 meV.

at low temperature, highlighting a supplementary phonon sideband for these emitters. On the other hand, the symmetry of the ZPL for group 2 is maintained at low temperature.

We now turn back to the range of ZPL energies observed within each group shown in Figure 3b,c. It is well-known that strain can induce shifts in the electronic structure and hence the optical transitions.[34] Such effects can be modeled using density functional theory (DFT) simulations, which we therefore used to calculate the optical response of a monolayer of hBN that contains the NBVN defect described in detail in ref 1 and has similar photophysical properties to emitters in Group 2 of the present study. The DFT calculations (see Figure S6) show that the range of ZPL positions expected from 5% strain is comparable to that observed in each of the two emitter groups shown in Figure 3. These results are in accord with strain induced exciton shifts that were observed for other 2D transition metal dichalcogenites, where strains of 3% resulted in 100 meV spectral shifts.[35,36] Nonetheless, we acknowledge that the magnitude of strain needed to account for the entire observed range of ZPL positions within each group is high, and other effects such as variations in the dielectric environment of the emitters are likely to contribute to the observed shifts.

CONCLUSION

In conclusion, we present two robust methodologies to engineer room-temperature multicolor single photon emission, based on annealing and electron beam irradiation. Moreover, we show that the emitters are stable even after annealing in harsh gaseous environments such as oxygen, hydrogen, and ammonia. By analyzing spectral features of these emitters, we could infer that there are at least two groups of defects. Although the emitters in the two groups exhibit significant differences in their spectral characteristics, they share similar local phonon energies and therefore are likely to have similar chemical structure. Our work may help open up possibilities for employing quantum emitters in 2D materials for emerging applications in nanophotonics and nanoscale sensing devices.

METHODS

Annealing hBN Flakes under Different Gas Environment. Grid-marked native oxide Si (100) substrates were cleaned by ultrasonication in acetone and ethanol combined with light mechanical abrasion. Samples were prepared by drop-casting 100 μL of ethanol/water solution containing ~200 nm pristine h-BN flakes (Graphene Supermarket) onto marked substrates and allowed to dry.

Argon and O_2 annealing was carried out in a tube furnace (Lindberg Blue). The tube furnace was evacuated to low vacuum (~10^{-3} Torr) by means of a scroll pump then purged for 30 min under 10 sccm of Ar or O_2 flow with pressure regulated at 1 Torr. The substrate was then heated under 10 sccm of argon flow or 500 °C under 10 sccm of O_2 flow, held at a fixed temperature for 30 min, and then allowed to cool to room temperature under continuous gas flow.

H_2 and NH_3 annealing was carried out in a dedicated vacuum chamber. The chamber was evacuated to high vacuum (~10^{-8} Torr) by means of a turbo molecular pump then purged for 30 min under 10 sccm of H_2 and NH_3 flow, respectively, with pressure regulated at 40 Torr. The substrate was then heated to 500 °C under 10 sccm H_2 or NH_3 flow, held at this temperature for 30 min, and then allowed to cool to room temperature under continuous gas flow.

Electron Beam Irradiation. The substrates prepared for electron beam irradiation underwent photolithography procedures and subsequent metal deposition to create a hard mask grid. The substrates were then prepared as described above. The grid allowed for easy identification of areas to characterize optically before and after electron beam irradiation.

Electron beam irradiation experiments were performed in a variable-pressure FEI field emission gun scanning electron microscope. A low-vacuum environment of H_2O at a pressure of 8 Pa was used for all experiments. A focused beam was used in a raster scanning pattern to expose the hBN flakes as a function of time up to 1 h over an area of 600 μm^2. An accelerating voltage of 15 kV and beam current of 1.4 nA were used for all electron beam irradiation experiments.

Optical Characterization. A CW 532 nm laser (Gem 532, Laser Quantum Ltd.) was used for excitation and scanning. The laser was directed through a Glan-Taylor polarizer (Thorlabs Inc.) and a half waveplate and focused onto the sample using a high numerical aperture (NA = 0.9, Nikon) objective lens. Scanning was performed either using an X-Y piezo scanning mirror (FSM-300) or an X-Y-Z nanocube system (PI instruments). The collected light was filtered using a 532 nm dichroic mirror (532 nm laser BrightLine, Semrock) and an additional long pass filter (Semrock). The signal was then coupled into a graded index fiber, where the fiber aperture serves as a confocal pinhole. A fiber splitter was used to direct the light to a spectrometer (Acton SpectraPro, Princeton Instrument Inc.) or to two avalanche photodiodes (Excelitas Technologies) used for single photon counting. Correlation measurements were done using a time-correlated single photon counting module (PicoHarp300, PicoQuant). The presented $g^2(\tau)$ curves were not corrected for background luminescence. Lifetime measurements were performed using a 510 nm pulsed laser excitation source (PiL051X, Advanced Laser Diode Systems GmbH) with a 100 ps pulse width and a 20 MHz repetition rate. Low-temperature PL spectroscopy was done at 14 K using a closed cycle refrigerating system cryostat (Janis CCS-XG-M/204N).

Theoretical Calculation. VASP[38] calculations were performed using the generalized gradient approximation to the exchange–correlation functional proposed by Perdew, Burke, and Ernzerhof.[39] All calculations are spin-polarized and use the projector augmented wave pseudopotentials supplied with the VASP code. A plane-wave cutoff of 450 eV was used for all calculations, which is considerably higher than default values for the pseudopotentials used and represents a well-converged calculation. Pristine single-layer hBN was first geometry optimized using the conventional cell and a 21 × 21 × 1 Monkhurst–Pack reciprocal space grid to an energy tolerance of 0.01

DOI: 10.1021/acsnano.6b03602
ACS Nano 2016, 10, 7331–7338

eV. A vacuum spacing of 20 Å was used to separate periodic images of the single layer and to ensure interaction between the layers is negligible. Relaxation of the lattice vectors using a conjugate gradient approach or by hand plotting the energy as a function of lattice parameter give the same optimized unit cell. The computational conditions are clearly good enough that basis size effects are not important. The optimized lattice parameter is 2.5 Å, with a bond length of 1.447 Å. A 7 × 7 supercell was used for the defective hBN monolayers with the reciprocal space grid reduced by a corresponding amount to 3 × 3 × 1. Defect structures were reoptimized. The imaginary component of the frequency-dependent dielectric matrix was calculated in the random phase approximation neglecting local field effects; the method is explained in detail in ref 3.[40] The two orthogonal components of the dielectric tensor in the plane of the hBN monolayer are along and perpendicular to the axis of the N_BV_N defect.

A Gaussian smearing function is used with a small width of 0.05 eV. For the relatively large supercells used here, this should give good results. We have also tried the tetrahedron Blochl corrected and an order-1 Methfessel–Paxton, smearing function; the latter with a considerably larger width of 0.2 eV (the default settings for VASP) with effectively no change in the calculated optical properties.

ASSOCIATED CONTENT

Supporting Information

The Supporting Information is available free of charge on the ACS Publications website at DOI: 10.1021/acsnano.6b03602.

Supplementary figures (Figure S1–S6) and detailed DFT discussion for strain effect on optical active defects (PDF)

AUTHOR INFORMATION

Corresponding Authors

*E-mail: igor.aharonovich@uts.edu.au.
*E-mail: milos.toth@uts.edu.au.

Notes

The authors declare no competing financial interest.

ACKNOWLEDGMENTS

We thank Kerem Bray for technical help with the optical measurements and Fedor Jelezko for useful discussions. The work was supported in part by the Australian Research Council (project no. DP140102721), FEI Company and by the Air Force Office of Scientific Research, United States Air Force. I. A. is the recipient of an Australian Research Council Discovery Early Career Research Award (project no. DE130100592). I.A. acknowledges the support from AOARD grant FA2386-15-1-4044. G.G. acknowledges support by the Swiss National Science Foundation (SNSF). H.M. is a recipient of the Samsung Scholarship. Measurements were supported in part by the Center for Excitonics, Center for Excitonics, an Energy Frontier Research Center funded by the U.S. Department of Energy, Office of Science, Office of Basic Energy Sciences under award no. DE-SC0001088. G.G. was supported in part by the National Science Foundation EFRI 2-DARE, award abstract no. 1542863.

REFERENCES

(1) Tran, T. T.; Bray, K.; Ford, M. J.; Toth, M.; Aharonovich, I. Quantum Emission from Hexagonal Boron Nitride Monolayers. *Nat. Nanotechnol.* **2016**, *11*, 37–41.

(2) Caldwell, J. D.; Kretinin, A. V.; Chen, Y.; Giannini, V.; Fogler, M. M.; Francescato, Y.; Ellis, C. T.; Tischler, J. G.; Woods, C. R.; Giles, A. J.; Hong, M.; Watanabe, K.; Taniguchi, T.; Maier, S. A.; Novoselov, K. S. Sub-Diffractional Volume-Confined Polaritons in the Natural Hyperbolic Material Hexagonal Boron Nitride. *Nat. Commun.* **2014**, *5*, 5221.

(3) Dai, S.; Ma, Q.; Andersen, T.; McLeod, A. S.; Fei, Z.; Liu, M. K.; Wagner, M.; Watanabe, K.; Taniguchi, T.; Thiemens, M.; Keilmann, F.; Jarillo-Herrero, P.; Fogler, M. M.; Basov, D. N. Subdiffractional Focusing and Guiding of Polaritonic Rays in a Natural Hyperbolic Material. *Nat. Commun.* **2015**, *6*, 6963.

(4) Li, P.; Lewin, M.; Kretinin, A. V.; Caldwell, J. D.; Novoselov, K. S.; Taniguchi, T.; Watanabe, K.; Gaussmann, F.; Taubner, T. Hyperbolic Phonon-Polaritons in Boron Nitride for Near-Field Optical Imaging and Focusing. *Nat. Commun.* **2015**, *6*, 7507.

(5) Dai, S.; Fei, Z.; Ma, Q.; Rodin, A. S.; Wagner, M.; McLeod, A. S.; Liu, M. K.; Gannett, W.; Regan, W.; Watanabe, K.; Taniguchi, T.; Thiemens, M.; Dominguez, G.; Neto, A. H. C.; Zettl, A.; Keilmann, F.; Jarillo-Herrero, P.; Fogler, M. M.; Basov, D. N. Tunable Phonon Polaritons in Atomically Thin van der Waals Crystals of Boron Nitride. *Science* **2014**, *343*, 1125–1129.

(6) Dai, S.; Ma, Q.; Liu, M. K.; Andersen, T.; Fei, Z.; Goldflam, M. D.; Wagner, M.; Watanabe, K.; Taniguchi, T.; Thiemens, M.; Keilmann, F.; Janssen, G. C.; Zhu, S. E.; Jarillo-Herrero, P.; Fogler, M. M.; Basov, D. N. Graphene on Hexagonal Boron Nitride as a Tunable Hyperbolic Metamaterial. *Nat. Nanotechnol.* **2015**, *10*, 682–686.

(7) Watanabe, K.; Taniguchi, T.; Kanda, H. Direct-Bandgap Properties and Evidence for Ultraviolet Lasing of Hexagonal Boron Nitride Single Crystal. *Nat. Mater.* **2004**, *3*, 404–409.

(8) Cassabois, G.; Valvin, P.; Gil, B. Hexagonal Boron Nitride is an Indirect Bandgap Semiconductor. *Nat. Photonics* **2016**, *10*, 262–266.

(9) Tran, T. T.; Zachreson, C.; Berhane, A. M.; Bray, K.; Sandstrom, R. G.; Li, L. H.; Taniguchi, T.; Watanabe, K.; Aharonovich, I.; Toth, M. Quantum Emission from Defects in Single-Crystalline Hexagonal Boron Nitride. *Phys. Rev. Appl.* **2016**, *5*, 034005.

(10) Song, L.; Ci, L.; Lu, H.; Sorokin, P. B.; Jin, C.; Ni, J.; Kvashnin, A. G.; Kvashnin, D. G.; Lou, J.; Yakobson, B. I.; Ajayan, P. M. Large Scale Growth and Characterization of Atomic Hexagonal Boron Nitride Layers. *Nano Lett.* **2010**, *10*, 3209–3215.

(11) Rostami, H.; Asgari, R. Valley Zeeman Effect and Spin-valley Polarized Conductance in Monolayer MoS2 in a Perpendicular Magnetic Field. *Phys. Rev. B: Condens. Matter Mater. Phys.* **2015**, *91*, 075433.

(12) del Corro, E.; Botello-Mendez, A. R.; Gillet, Y.; Elías, A. L.; Terrones, H.; Feng, S.; Fantini, C.; Rhodes, D.; Pradhan, N. R.; Balicas, L. Atypical Exciton-Phonon Interactions in WS2 And WSe2Monolayers Revealed by Resonance Raman Spectroscopy. *Nano Lett.* **2016**, *16*, 2363–2368.

(13) Botsoa, J.; Sauvage, T.; Adam, M. P.; Desgardin, P.; Leoni, E.; Courtois, B.; Treussart, F.; Barthe, M. F. Optimal Conditions for NV– center Formation in Type-Ib Diamond Studied Using Photoluminescence and Positron Annihilation Spectroscopies. *Phys. Rev. B: Condens. Matter Mater. Phys.* **2011**, *84*, 125209.

(14) Orwa, J. O.; Santori, C.; Fu, K. M. C.; Gibson, B.; Simpson, D.; Aharonovich, I.; Stacey, A.; Cimmino, A.; Balog, P.; Markham, M.; Twitchen, D.; Greentree, A. D.; Beausoleil, R. G.; Prawer, S. Engineering of Nitrogen-Vacancy Color Centers in High Purity Diamond by Ion Implantation and Annealing. *J. Appl. Phys.* **2011**, *109*, 083530.

(15) Thiel, B. L.; Toth, M.; Schroemges, R. P. M.; Scholtz, J. J.; van Veen, G.; Knowles, W. R. Two-stage Gas Amplifier for Ultrahigh Resolution Low Vacuum Scanning Electron Microscopy. *Rev. Sci. Instrum.* **2006**, *77*, 033705.

(16) Toth, M.; Lobo, C. J.; Lysaght, M. J.; Vladár, A. E.; Postek, M. T. Contamination-Free Imaging by Electron Induced Carbon Volatilization in Environmental Scanning Electron Microscopy. *J. Appl. Phys.* **2009**, *106*, 034306.

(17) Cui, Z.; Oyer, A. J.; Glover, A. J.; Schniepp, H. C.; Adamson, D. H. Large Scale Thermal Exfoliation and Functionalization of Boron Nitride. *Small* **2014**, *10*, 2352–2355.

DOI: 10.1021/acsnano.6b03602
ACS Nano 2016, 10, 7331–7338

(18) Fu, K. M. C.; Santori, C.; Barclay, P. E.; Beausoleil, R. G. Conversion of Neutral Nitrogen-vacancy Centers to Negatively Charged Nitrogen-vacancy Centers Through Selective Oxidation. *Appl. Phys. Lett.* **2010**, *96*, 121907.
(19) Shanley, T. W.; Martin, A. A.; Aharonovich, I.; Toth, M. Localized Chemical Switching of the Charge State of Nitrogen-vacancy Luminescence Centers in Diamond. *Appl. Phys. Lett.* **2014**, *105*, 063103.
(20) Pezzagna, S.; Rogalla, D.; Wildanger, D.; Meijer, J.; Zaitsev, A. Creation and Nature of Optical Centres in Diamond for Single-photon Emission—Overview and Critical Remarks. *New J. Phys.* **2011**, *13*, 035024.
(21) Nakamura, S.; Iwasa, N.; Senoh, M.; Mukai, T. Hole Compensation Mechanism of P-Type GaN Films. *Jpn. J. Appl. Phys.* **1992**, *31*, 1258.
(22) Gutiérrez, H. R.; Perea-López, N.; Elías, A. L.; Berkdemir, A.; Wang, B.; Lv, R.; López-Urías, F.; Crespi, V. H.; Terrones, H.; Terrones, M. Extraordinary Room-Temperature Photoluminescence in Triangular WS2Monolayers. *Nano Lett.* **2013**, *13*, 3447−3454.
(23) Michler, P.; Kiraz, A.; Becher, C.; Schoenfeld, W. V.; Petroff, P. M.; Zhang, L.; Hu, E.; Imamoglu, A. A Quantum Dot Single-photon Turnstile Device. *Science* **2000**, *290*, 2282−2285.
(24) Zaitsev, A. M. Vibronic Spectra of Impurity-related Optical Centers in Diamond. *Phys. Rev. B: Condens. Matter Mater. Phys.* **2000**, *61*, 12909.
(25) Huxter, V. M.; Oliver, T. A. A.; Budker, D.; Fleming, G. R. Vibrational and Electronic Dynamics of Nitrogen−Vacancy Centres in Diamond Revealed by Two-dimensional Ultrafast Spectroscopy. *Nat. Phys.* **2013**, *9*, 744−749.
(26) Kurtsiefer, C.; Mayer, S.; Zarda, P.; Weinfurter, H. Stable Solid-state Source of Single Photons. *Phys. Rev. Lett.* **2000**, *85*, 290−293.
(27) Neitzke, O.; Morfa, A.; Wolters, J.; Schell, A. W.; Kewes, G.; Benson, O. Investigation of Line Width Narrowing and Spectral Jumps of Single Stable Defect Centers in ZnO at Cryogenic Temperature. *Nano Lett.* **2015**, *15*, 3024−3029.
(28) Bernard, J.; Fleury, L.; Talon, H.; Orrit, M. Photon Bunching in the Fluorescence from Single Molecules: A Probe for Intersystem Crossing. *J. Chem. Phys.* **1993**, *98*, 850−859.
(29) Fleury, L.; Segura, J. M.; Zumofen, G.; Hecht, B.; Wild, U. P. Nonclassical Photon Statistics in Single-Molecule Fluorescence at Room Temperature. *Phys. Rev. Lett.* **2000**, *84*, 1148−1151.
(30) Castelletto, S.; Johnson, B. C.; Zachreson, C.; Beke, D.; Balogh, I.; Ohshima, T.; Aharonovich, I.; Gali, A. Room Temperature Quantum Emission from Cubic Silicon Carbide Nanoparticles. *ACS Nano* **2014**, *8*, 7938−7947.
(31) Neu, E.; Agio, M.; Becher, C. Photophysics of Single Silicon Vacancy Centers in Diamond: Implications for Single Photon Emission. *Opt. Express* **2012**, *20*, 19956−19971.
(32) Aharonovich, I.; Castelletto, S.; Simpson, D. A.; Greentree, A. D.; Prawer, S. Photophysics of Chromium-related Diamond Single-photon Emitters. *Phys. Rev. A: At., Mol., Opt. Phys.* **2010**, *81*, 043813.
(33) Berthel, M.; Mollet, O.; Dantelle, G.; Gacoin, T.; Huant, S.; Drezet, A. Photophysics of Single Nitrogen-vacancy Centers in Diamond Nanocrystals. *Phys. Rev. B: Condens. Matter Mater. Phys.* **2015**, *91*, 035308.
(34) Neu, E.; Fischer, M.; Gsell, S.; Schreck, M.; Becher, C. Fluorescence and Polarization Spectroscopy of Single Silicon Vacancy Centers in Heteroepitaxial Nanodiamonds on Iridium. *Phys. Rev. B: Condens. Matter Mater. Phys.* **2011**, *84*, 205211.
(35) Castellanos-Gomez, A.; Roldan, R.; Cappelluti, E.; Buscema, M.; Guinea, F.; van der Zant, H. S.; Steele, G. A. Local Strain Engineering in Atomically Thin MoS2. *Nano Lett.* **2013**, *13*, 5361−5366.
(36) Desai, S. B.; Seol, G.; Kang, J. S.; Fang, H.; Battaglia, C.; Kapadia, R.; Ager, J. W.; Guo, J.; Javey, A. Strain-Induced Indirect to Direct Bandgap Transition in Multilayer WSe2. *Nano Lett.* **2014**, *14*, 4592−4597.
(37) Jungwirth, N. R.; Calderon, B.; Ji, Y.; Spencer, M. G.; Flatté, M. E.; Fuchs, G. D. Temperature Dependence of Wavelength Selectable Zero-Phonon Emission from Single Defects in Hexagonal Boron Nitride ArXiv e-prints. 2016, arXiv:1605.04445.
(38) Kresse, G.; Hafner, J. Ab Initio Molecular-Dynamics Simulation of the Liquid-Metal-Amorphous-Semiconductor Transition in Germanium. *Phys. Rev. B: Condens. Matter Mater. Phys.* **1994**, *49*, 14251.
(39) Perdew, J. P.; Burke, K.; Ernzerhof, M. Generalized Gradient Approximation Made Simple. *Phys. Rev. Lett.* **1996**, *77*, 3865−3868.
(40) Gajdoš, M.; Hummer, K.; Kresse, G.; Furthmüller, J.; Bechstedt, F. Linear Optical Properties in the Projector-augmented Wave Methodology. *Phys. Rev. B: Condens. Matter Mater. Phys.* **2006**, *73*, 045112.

NOTE ADDED IN PROOF

During the review of this manuscript a related work appeared on arxiv.[37]

DOI: 10.1021/acsnano.6b03602
ACS Nano 2016, 10, 7331−7338